Nanoscale Advances

ROYAL SOCIETY OF CHEMISTRY

PAPER

View Article Online
View Journal | View Issue

Cite this: *Nanoscale Adv.*, 2023, **5**, 6626

Infrared spectroscopic study of solvation and size effects on reactions between water molecules and neutral rare-earth metals†

Tiantong Wang,[ab] Shangdong Li,[ab] Wenhui Yan,[ab] Shuai Jiang,[ab] Hua Xie,[a] Gang Li *[a] and Ling Jiang *[ac]

Received 11th October 2023
Accepted 25th October 2023

DOI: 10.1039/d3na00873h

rsc.li/nanoscale-advances

Elucidating the solvation and size effects on the reactions between water and neutral metals is crucial for understanding the microscopic mechanism of the catalytic processes but has been proven to be a challenging experimental target due to the difficulty in size selection. Here, MO_4H_6 and $M_2O_6H_7$ (M = Sc, Y, La) complexes were synthesized using a laser–vaporization cluster source and characterized by size-specific infrared-vacuum ultraviolet spectroscopy combined with quantum chemical calculations. The MO_4H_6 and $M_2O_6H_7$ complexes were found to have $H^{\bullet}M(OH)_3(H_2O)$ and $M_2(\mu_2\text{-}OH)_2(\eta^1\text{-}OH)_3(\eta^1\text{-}OH_2)$ structures, respectively. A combination of experiments and theory revealed that the formation of $H^{\bullet}M(OH)_3(H_2O)$ and $M_2(\mu_2\text{-}OH)_2(\eta^1\text{-}OH)_3(\eta^1\text{-}OH_2)$ is both thermodynamically exothermic and kinetically facile in the gas phase. The results indicated that upon the addition of water to $H^{\bullet}M(OH)_3$, the feature of the hydrogen radical is retained. In the processes from mononuclear $H^{\bullet}M(OH)_3$ to binuclear $M_2(\mu_2\text{-}OH)_2(\eta^1\text{-}OH)_3(\eta^1\text{-}OH_2)$, the active hydrogen atom undergoes the evolution from hydrogen radical → bridging hydrogen → metal hydride → hydrogen bond, which is indicative of a reduced reactivity. The present system serves as a model for clarifying the solvation and size effects on the reactions between water and neutral rare-earth metals and offers a general paradigm for systematic studies on a broad class of the reactions between small molecules and metals at the nanoscale.

1 Introduction

Rare-earth metals (Sc, Y, Ln) and their complexes have been widely used in various catalytic processes.[1–3] For instance, Ni@CeO_2-doped MgH_2 hydrogen storage material reduces the dehydrogenation activation energy by 20.3 kcal mol^{-1}, which significantly improves the hydrogen release property of MgH_2 material.[4–6] Rare-earth single-atom catalysts (SAC) are extensively exploited in the photocatalytic/electrocatalytic processes of O_2/CO_2/N_2, *etc.*[7–12] Theoretical studies have verified that in the electrocatalytic reduction of O_2, the rare-earth SAC undergoes the transformation from the poly-hydroxyl structure to the solvated water structure.[9,13] CeO_2 is utilized as the catalyst in the hydrogenation reduction of alkenes/alkynes,[14] in which the key intermediates contain important metal hydride structures and poly-hydroxyl structures. Ultrathin 2D rare-earth nanomaterials of the layered rare-earth hydroxides were synthesized in solution[15,16] and were confirmed to exhibit great potential in various applications, such as optoelectronics,[17] magnetic devices,[18] and high-efficiency catalysts.[19] Therefore, the studies on the reactions between small molecules and rare-earth metals at the cluster scale are expected to provide microscopic information to unravel the structure–reactivity relationship of catalysts.

Various efforts have been devoted to the spectroscopic studies of the reactions of water molecules with rare-earth metals[20–27] owing to their important roles in renewable sources and transport/storage of hydrogen energy.[28,29] The investigation of the solvation and size effects on the reactions between water with neutral metals is crucial to understanding the microscopic mechanism of catalytic processes but has been proven to be a challenging experimental target due to the difficulty in size selection. Matrix-isolation infrared spectroscopy has provided valuable insights into the reactions of neutral single rare-earth metal atoms with water, suggesting the formation of the inserted HMOH structures and the solvated $M(H_2O)_{1-2}$ structures.[20,24,26,27] Recently, we have characterized two different types of rare-earth hydroxides (MO_3H_4 and $M_2O_4H_4$ (M = Sc, Y, La))[30,31] using size-specific infrared-vacuum ultraviolet (IR-VUV) spectroscopy, in which MO_3H_4 has a hydrogen radical structure and $M_2O_4H_4$ has a water-split structure. In this work, we increased the number of water

[a]State Key Laboratory of Molecular Reaction Dynamics, Dalian Institute of Chemical Physics, Chinese Academy of Sciences, Dalian 116023, China. E-mail: gli@dicp.ac.cn; ljiang@dicp.ac.cn

[b]University of Chinese Academy of Sciences, Beijing 100049, China

[c]Hefei National Laboratory, Hefei 230088, China

† Electronic supplementary information (ESI) available. See DOI: https://doi.org/10.1039/d3na00873h

molecules to study the solvation and size effects on the reactions between water with neutral rare-earth metals. Two new rare-earth metal hydroxides with the chemical formulas MO_4H_6 and $M_2O_6H_7$ (M = Sc, Y, La) were prepared and characterized by IR-VUV spectroscopy and quantum chemical calculation. MO_4H_6 and $M_2O_6H_7$ complexes were found to have the $H^{\bullet}M(OH)_3(H_2O)$ and $M_2(\mu_2\text{-}OH)_2(\eta^1\text{-}OH)_3(\eta^1\text{-}OH_2)$ structures, respectively, in which the hydrogen radical features were retained with the solvation of water in the mononuclear complex MO_4H_6 and the reactivity of the active hydrogen was reduced in the formation processes of binuclear complex $M_2O_6H_7$.

2 Experimental and theoretical methods

The experiment was performed using the IR-VUV apparatus, which has been described in detail in previous reports.[32–34] Neutral MO_4H_6 and $M_2O_6H_7$ (M = Sc, Y, La) complexes were prepared using the laser–vaporization cluster source in a pulsed supersonic expansion of 0.2% H_2O/helium. The second harmonic of a Nd: YAG laser (532 nm) was employed to ablate the metal target, with a pulse energy of 1.0 mJ. The reaction gas was introduced using a Parker pulse valve (Series 009), with a pulse width of 180 μs. The molecular beams that passed through a 4 mm-diameter skimmer were ionized by a VUV laser and then detected by a reflectron time-of-flight mass spectrometer (TOF-MS).

VUV light with a wavelength of 193 nm was produced by an ArF excimer laser (COMPex 50 F, Coherent, Germany), with an energy of 14 mJ per pulse. The infrared laser was delivered by a potassium titanyl phosphate/potassium titanyl arsenate optical parametric oscillator/amplifier system (OPO/OPA, LaserVision) pumped by another seeded Nd: YAG laser (Continuum, Surelite EX). The OPO/OPA system was tunable from 700 to 7000 cm^{-1}, with a line width of 1 cm^{-1}.

The pulse valve, the vaporization laser, and VUV light were operated at 20 Hz. The tunable IR light pulse was introduced at approximately 150 ns prior to the VUV pulse in a crossed manner and operated at 10 Hz. When the resonant vibrational transition was irradiated by the IR laser light and caused vibrational predissociation, a depletion of a selected neutral cluster mass signal was detected. The infrared spectra were recorded from the difference between the mass spectral signals with and without the infrared laser (IR laser ON minus IR laser OFF). The IR spectra of the size-selected neutral MO_4H_6 and $M_2O_6H_7$ complexes were obtained from the depletion spectrum of the ion signal intensity as a function of the IR wavelength. Typical spectra were recorded by scanning the IR wavelength in the steps of 2 cm^{-1} and averaging over 400 laser shots at each wavelength. The infrared wavelength was calibrated using a commercial wavelength meter (HighFinesse GmbH, WS6-200 VIS IR).

Quantum chemical calculations were performed using the Gaussian 16 package[35] at the TPSSh/def2-TZVP level of theory. Our test calculations indicated that the TPSSh functional has a lower computational cost than B2PLYPD3 and a better computational performance in the spectra and energetics than B3LYP for MO_4H_6 and $M_2O_6H_7$ (M = Sc, Y, La). Accordingly, we chose the TPSSh functional instead of the B2PLYPD3 or B3LYP functionals that we used in previous works.[30,31] For the possible isomerization paths, the initial structures of the transition states were constructed manually and optimized in the Berny algorithm. Intrinsic reaction coordinates (IRC) of all the transition states were carried out to confirm that the transition states were connected to the initial and final states. The relative energies and energy barriers were calculated for 0 K structures, including the zero-point vibrational corrections. The harmonic vibrational frequencies were scaled by a factor of 0.968 in order to account for the method-dependent systematic errors.[36] The resulting stick spectra were convoluted by a Gaussian line shape function with a 15 cm^{-1} width at half-maximum (FWHM).

3 Results and discussion

As exemplified by the Sc + H_2O reaction, the mass spectrum of the species is shown in Fig. S1.† The experimental IR spectra of neutral MO_4H_6 and $M_2O_6H_7$ (M = Sc, Y, La) complexes in the OH stretching region are shown in Fig. 1a–c and 2a–c, respectively. The experimental band positions of MO_4H_6 and $M_2O_6H_7$ (M = Sc, Y, La) are listed in Tables S1 and S2,† respectively. As shown in Fig. 1a–c, the experimental IR spectrum of each MO_4H_6 complex comprises three groups of bands (labeled bands A, B, and C). B and A in the IR spectra of ScO_4H_6, YO_4H_6, and LaO_4H_6 are centered at 3398, 3104, and 2952 cm^{-1}, respectively, indicating redshift down through the group 3 metal of the periodic table. The B bands in the IR spectrum of ScO_4H_6, YO_4H_6, and LaO_4H_6 are observed at 3694, 3704, and 3722 cm^{-1}, respectively, showing a slight blueshift down through the group 3 metal of the periodic table. B and C in the IR spectra of ScO_4H_6, YO_4H_6, and LaO_4H_6 are located at 3786, 3784, and 3748 cm^{-1}, respectively, showing a slight redshift down through the group 3 metals of the periodic table. Similar spectral features were observed for $M_2O_6H_7$ (labeled bands a, b, and c), except for the absence of band a in $Sc_2O_6H_7$.

To understand the experimental IR spectra and identify the structures of MO_4H_6 and $M_2O_6H_7$ (M = Sc, Y, La) complexes, quantum chemical calculations were carried out at the TPSSh/def2-TZVP level of theory. The structures of the identified isomers and the comparison of their calculated IR spectra with the experimental ones are shown in Fig. 1 and 2, respectively. The structures of other low-lying isomers and the comparison of their calculated IR spectra with the experimental ones are illustrated in Fig. S2 and S3,† respectively.

As shown in Fig. S2,† the most stable isomer of ScO_4H_6 (labeled 1A) has a $Sc(OH)_2(H_2O)_2$ structure with a doublet electronic ground state, in which the scandium hydroxide $Sc(OH)_2$ are solvated with two water molecules. The 1B isomer has a $H^{\bullet}Sc(OH)_3(H_2O)$ structure with the involvement of a hydrogen radical, as evidenced by the calculated Mulliken spin densities [H(0), 0.72; Sc(0), 0.10] (for the labeling of the atoms, see Table S1†). The 1B isomer lies slightly higher in energy than the 1A isomer by 2.6 kcal mol^{-1}. The 1C isomer lies

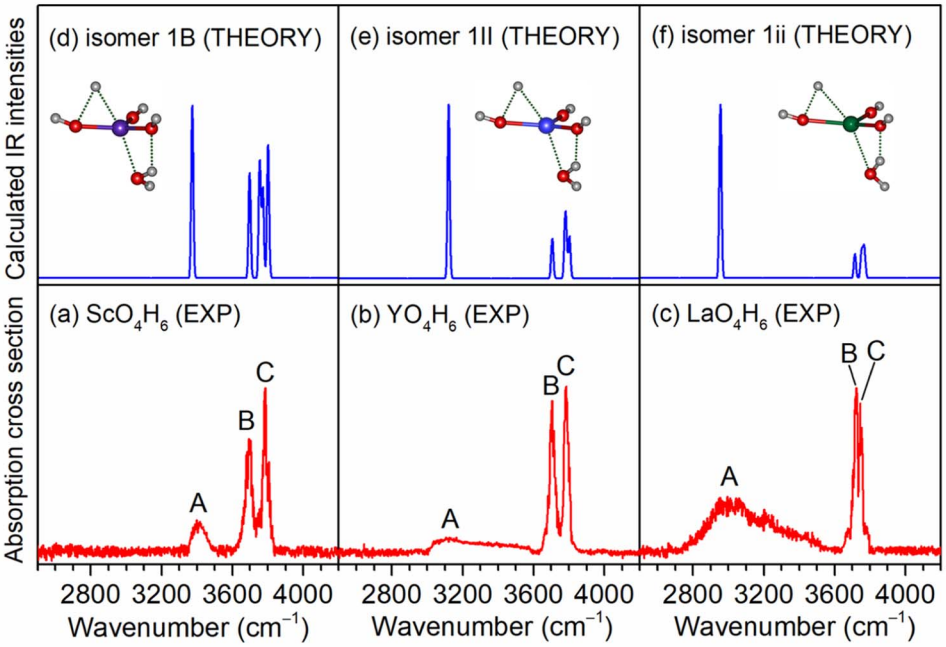

Fig. 1 Comparison of the experimental IR spectra of neutral MO_4H_6 complexes (M = Sc, Y, La) (a–c) and calculated IR spectra of isomers 1B, 1II, and 1ii (d–f). Calculations were performed at the TPSSh/def2-TZVP level of theory, with the harmonic vibrational frequencies scaled by a factor of 0.968. The structures are embedded in the inset (O, red; H, light gray; Sc, purple; Y, blue; La, olive).

36.0 kcal mol^{-1} above the 1A isomer and has a $ScO(H_2O)_3$ structure, in which three water molecules are weakly bound to ScO. It can be seen from Fig. S2† that the calculated IR spectrum of the isomer 1B agrees best with the experimental one. As listed in Table S1,† the calculated band at 3374 cm^{-1} is attributed to the symmetric stretching mode of the O(4)H(4) and O(4)H(5) groups, which is consistent with the experimental band A (3398 cm^{-1}); the antisymmetric stretching mode of the O(4)H(4) and O(4)H(5) groups was calculated to be 3698 cm^{-1}, which is in accordance with the experimental band B (3694 cm^{-1}); the

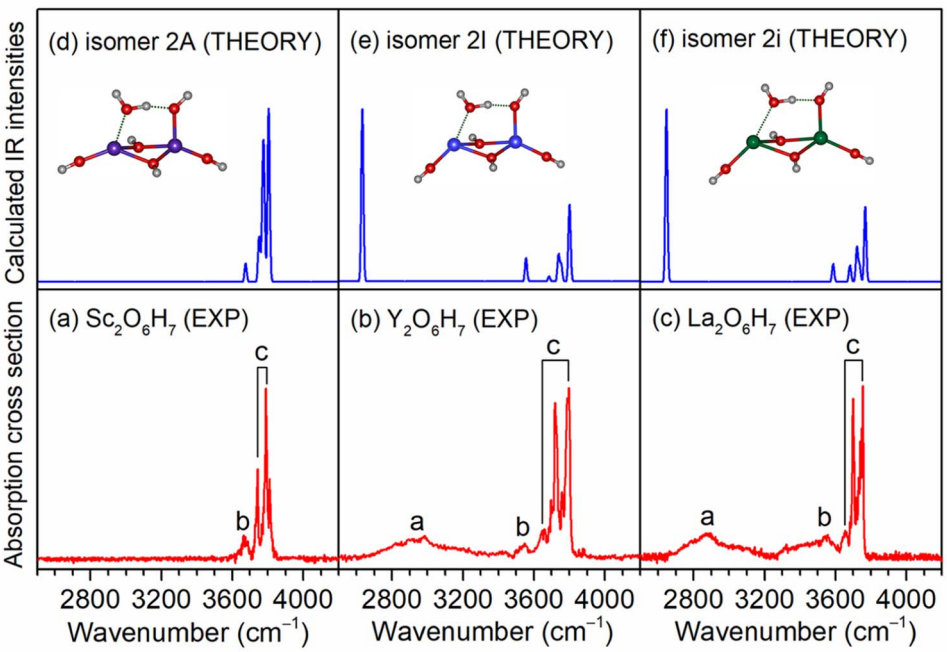

Fig. 2 Comparison of the experimental IR spectra of neutral $M_2O_6H_7$ complexes (M = Sc, Y, La) (a–c) and the calculated IR spectra of isomers 2A, 2I, and 2i (d–f). Calculations were performed at the TPSSh/def2-TZVP level of theory, with the harmonic vibrational frequencies scaled by a factor of 0.968. The structures are embedded in the inset (O, red; H, light gray; Sc, purple; Y, blue; La, olive).

stretching modes of the O(1)H(1), O(2)H(2), and O(3)H(3) groups were calculated to 3802, 3772, and 3758 cm^{-1}, respectively, which were observed as one band in the experimental spectrum (band C, 3786 cm^{-1}). However, the calculated IR spectrum of the isomer 1A (Fig. S1b†) consists of the bands at 2693 and 2955 cm^{-1}, corresponding to the hydrogen-bonded OH stretching modes of the solvated water molecules, which are not observed experimentally. Analogously, the presence of isomer 1C can be ruled out based on the calculated band at 2640 cm^{-1}. Similar results are also obtained for the YO_4H_6 and LaO_4H_6 complexes (Fig. S2 and Table S1†). As summarized in Fig. 1, the agreement of the simulated IR spectra of the 1B, 1II, and 1ii isomers with the experimental spectra of ScO_4H_6, YO_4H_6, and LaO_4H_6 is reasonable to identify the presence of $H^{\bullet}M(OH)_3(H_2O)$ (M = Sc, Y, La) structures.

For $Sc_2O_6H_7$, the most stable isomer (labeled 2A) has a $Sc_2(\mu_2\text{-}OH)_2(\eta^1\text{-}OH)_3(\eta^1\text{-}OH_2)$ structure with a doublet electronic ground state (Fig. S3d†), in which one water molecule forms one weakly bond with one scandium hydroxide and one hydrogen-bond with the hydroxyl group of another scandium hydroxide. The 2B isomer has a similar structure and lies only 0.1 kcal mol^{-1} above 2A, in which one water molecule forms one weak bond with one scandium hydroxide and one hydrogen bond with the hydroxyl group of the same scandium hydroxide. In the calculated IR spectrum of isomer 2A (Fig. S3 and Table S2†), the band at 3675 cm^{-1} is attributed to the stretching mode of the O(6)H(6) group, which is consistent with the experimental band b (3662 cm^{-1}); the stretching modes of the O(n)H(n) (n = 1–5) groups is calculated to 3806, 3804, 3778, 3770, and 3751 cm^{-1}, respectively, which are observed in the experimental spectrum at 3810, 3788, and 3742 cm^{-1} (band c). The absence of stretching mode of the O(6)H(7) group (2474 cm^{-1}) (Table S2†) could be rationalized that the photon energy of the IR laser in this wavelength region is not sufficient to cause the vibrational predissociation of $Sc_2O_6H_7$. In the calculated IR spectrum of the isomer 2B (Fig. S3g†), the hydrogen-bonded OH stretching mode of the solvated water molecule is predicted at 3275 cm^{-1}, which is not observed in the experimental spectrum. As summarized in Fig. 2, the agreement of the simulated IR spectra of the 2A, 2I, and 2i isomers with the experimental spectra is reasonable to confirm the $M_2(\mu_2\text{-}OH)_2(\eta^1\text{-}OH)_3(\eta^1\text{-}OH_2)$ (M = Sc, Y, La) structures responsible for $Sc_2O_6H_7$, $Y_2O_6H_7$, and $La_2O_6H_7$.

Considering that the reactions in the laver–vaporization processes are quite intricate and their intermediates are very difficult to characterize experimentally, quantum chemical calculations were performed to explore the possible reaction mechanisms. Due to the similarities in the IR spectra and structures of MO_4H_6 and $M_2O_6H_7$ (M = Sc, Y, La) complexes, we used ScO_4H_6 and $Sc_2O_6H_7$ as examples to investigate the possible formation pathways. Previous studies have demonstrated that the Sc + H_2O → Sc(H_2O) reaction is more favorable than the dimerization of Sc atoms.[31] As shown in Fig. S1,† the mononuclear complexes (*i.e.*, Sc, ScO, HScO, Sc$(OH)_2$, and $H^{\bullet}Sc(OH)_3$) were observed in the mass spectrum, for which the formation mechanisms have been reported previously.[20,23,25,30] Consequently, we will mainly discuss the dominant pathways that begin from the mononuclear complexes.

The potential energy profiles for the formation of ScO_4H_6 (isomer 1B) initiated by the reaction of ScO with H_2O are shown in Fig. 3. ScO reacts with the first water molecule to form a solvation structure Sc$O(H_2O)$, which is predicted to be exothermic by 18.5 kcal mol^{-1} at the TPSSh/def2-TZVP level of theory. The Sc$O(H_2O)$ → Sc$(OH)_2$ isomerization is highly exothermic by 41.3 kcal mol^{-1} *via* a transition state (TS1) with a very small barrier of 1.1 kcal mol^{-1}. The addition of H_2O to Sc$(OH)_2$ forms Sc$(OH)_2(H_2O)$, which could undergo isomerization to $H^{\bullet}Sc(OH)_3$. TS2 lies below the energy of Sc$(OH)_2$ + H_2O reactants by 14.4 kcal mol^{-1}. Sc$(OH)_2$ + H_2O → $H^{\bullet}Sc(OH)_3$ overall reaction is exothermic by 16.1 kcal mol^{-1} and is thus thermodynamically favorable. The mechanism for kinetically trapping $H^{\bullet}Sc(OH)_3$ by the soft helium expansion has been recently discussed in detail.[30] The $H^{\bullet}Sc(OH)_3$ complex combines with the water molecule to form the target product ScO_4H_6 ($H^{\bullet}Sc(OH)_3(H_2O)$, isomer 1B), which is exothermic by 16.3 kcal mol^{-1}.

Fig. 4 shows the potential energy profiles for the formation of $Sc_2O_6H_7$ (isomer 2A) initiated from the mononuclear non-radical complexes. The ScO + HScO → HSc_2O_2 reaction is predicted to be extremely exothermic at 106.1 kcal mol^{-1}. The most stable isomer of HSc_2O_2 has a $Sc_2(\mu_2\text{-}O)_2(\eta^1\text{-}H)$ structure, which combines with one water molecule to form IM1 and IM2. IM1 can be isomerized to IM5 *via* TS4. The calculated energy of TS4 is lower than that of IM1, which is due to the zero-point energy correction.[37–39] This indicates that the energy barrier for the IM1 → IM5 isomerization is very low. IM5 undergoes

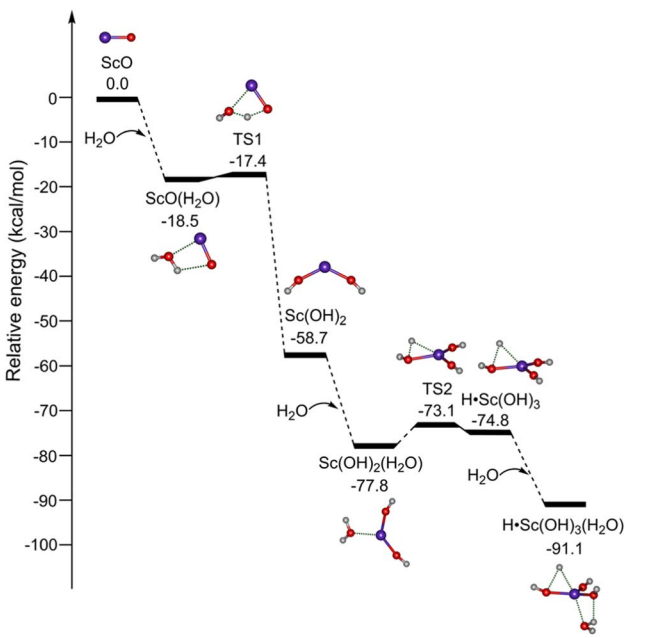

Fig. 3 Potential energy profiles for the formation of ScO_4H_6 ($H^{\bullet}Sc(OH)_3(H_2O)$, isomer 1B). The abbreviation "TS" denotes the transition state. Calculations were performed at the TPSSh/def2-TZVP level of theory. Corresponding structures are embedded in the inset (O, red; H, light gray; Sc, purple).

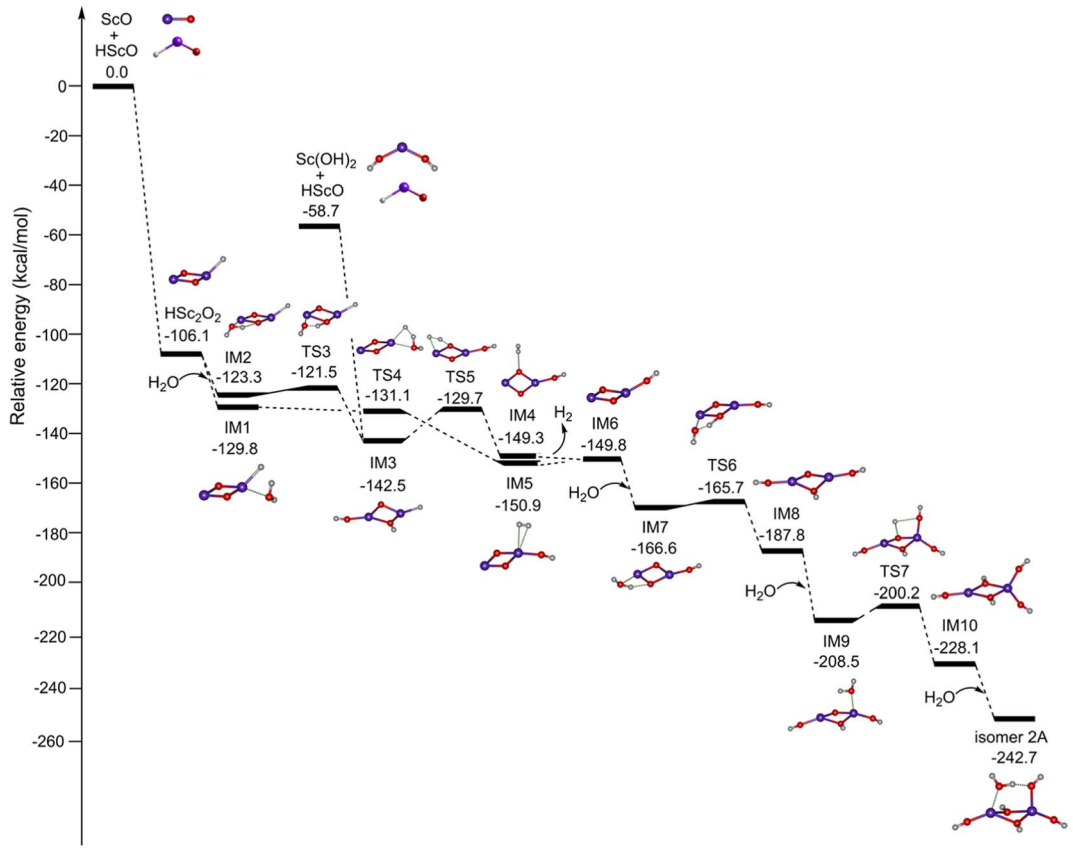

Fig. 4 Potential energy profiles for the formation of $Sc_2O_6H_7$ (isomer 2A) initiated from the mononuclear non-radical complexes. The abbreviation "IM" stands for intermediate and "TS" for the transition state. Calculations were performed at the TPSSh/def2-TZVP level of theory. Corresponding structures are embedded in the inset (O, red; H, light gray; Sc, purple).

dehydrogenation to form IM6 with a slightly endothermic value of 1.1 kcal mol^{-1}, which could be compensated by the highly exothermic overall reaction of $HSc_2O_2 + H_2O \rightarrow IM6 + H_2$. Similarly, the reaction path of IM2 → TS3 → IM3 → TS5 → IM4 → IM6 is also both thermodynamically and kinetically facile in the gas phase. IM3 could also be generated by the combination of $Sc(OH)_2$ and HScO, which is predicted to be highly exothermic by 83.8 kcal mol^{-1}. The addition of H_2O to IM6 forms IM7, which is exothermic by 16.8 kcal mol^{-1}. IM7 undergoes isomerization to the most stable hydroxyl structure IM8 *via* TS6 with a tiny barrier of 0.9 kcal mol^{-1}. IM8 reacts with the second water molecule to form IM9, which is exothermic by 20.7 kcal mol^{-1}. IM9 can be isomerized to an all-hydroxyl structure IM10 *via* TS7 with a barrier of 8.3 kcal mol^{-1}. The addition of the third water molecule to IM10 generates the target product $Sc_2O_6H_7$ (isomer 2A), which is exothermic by 14.6 kcal mol^{-1}.

Considering that $H^{\bullet}Sc(OH)_3$ and OH radicals are also generated in the laser–vaporization process,[30,34] $Sc_2O_6H_7$ might also be formed *via* reactions (1) and (2).

$$H^{\bullet}Sc(OH)_3 + Sc \rightarrow Sc_2O_3H_4 \quad (1)$$

$$Sc_2O_3H_4 + 3OH \rightarrow Sc_2O_6H_7 \quad (2)$$

Accordingly, the potential energy profiles for the formation of $Sc_2O_6H_7$ initiated from the mononuclear radical complexes are shown in Fig. 5. $H^{\bullet}Sc(OH)_3$ reacts with the Sc atom to produce the binuclear complex IM11; the reaction is predicted to be highly exothermic by 97.3 kcal mol^{-1}. IM11 can be isomerized to IM12 *via* TS8 with a small barrier of 1.6 kcal mol^{-1}. The reaction of IM12 with the first, second, and third OH radicals is predicted to be extremely exothermic by 128.4, 122.2, and 51.3 kcal mol^{-1}, respectively. The subsequent isomerization from IM15 to isomer 2B is exothermic by 1.2 kcal mol^{-1} *via* TS9 with a barrier of 9.3 kcal mol^{-1}. Isomer 2B can be further isomerized to form the most stable isomer 2A *via* TS10 with a small barrier of 3.8 kcal mol^{-1}. Consequently, the formation of isomer 2A is both thermodynamically exothermic and kinetically facile in the gas phase, which is consistent with the experimental observation.

The reaction mechanisms of rare-earth metals with water molecules can be inferred from the aforementioned formation pathways of ScO_4H_6 and $Sc_2O_6H_7$. Mononuclear rare-earth metal oxide (MO (M = Sc, Y, La)) could induce the decomposition of water molecules until the hydrogen-radical adduct $H^{\bullet}M(OH)_3$ was generated. The addition of the subsequent water molecule forms the solvated complex $H^{\bullet}M(OH)_3(H_2O)$. The binuclear complex M_2O_3H (labeled IM6 in Fig. 4) might also induce the successive decomposition of water molecules to

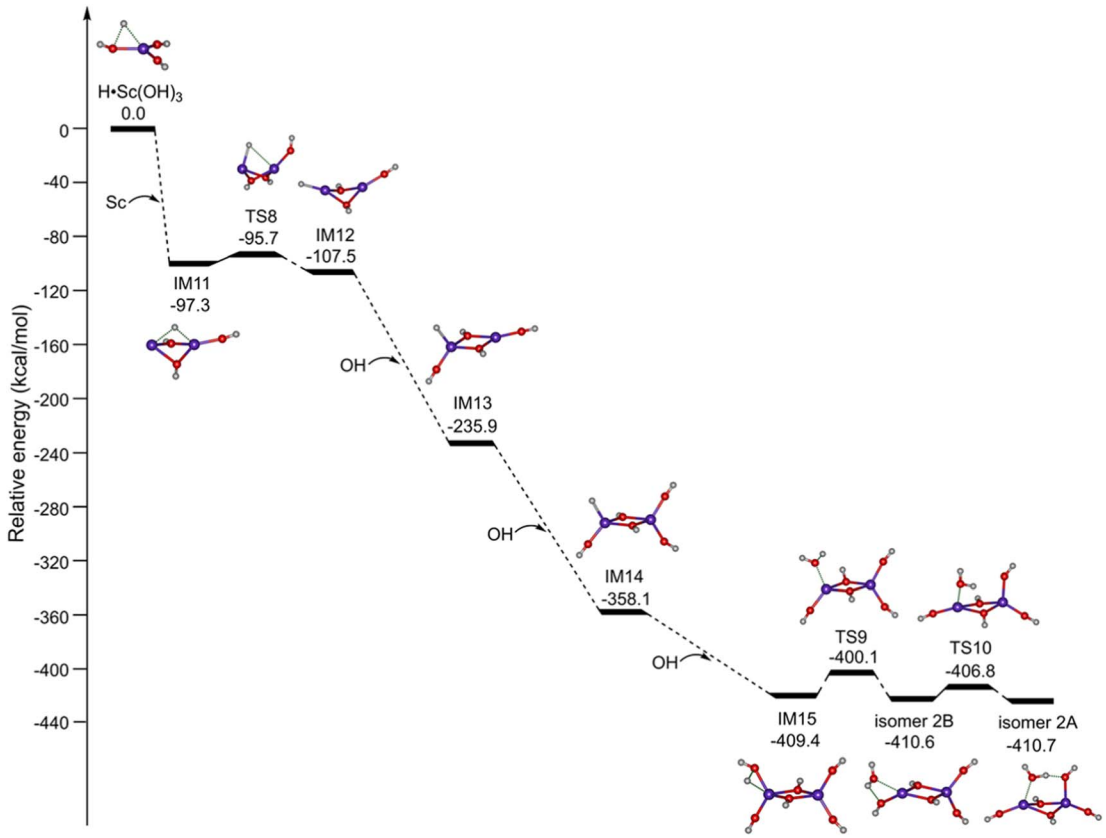

Fig. 5 Potential energy profiles for the formation of $Sc_2O_6H_7$ (isomer 2A) initiated from the mononuclear radical complexes. The abbreviation "IM" stands for intermediate and "TS" for the transition state. Calculations were performed at the TPSSh/def2-TZVP level of theory. Corresponding structures are embedded in the inset (O, red; H, light gray; Sc, purple).

produce the poly-hydroxyl complex $M_2O_5H_5$ (labeled IM10 in Fig. 4). The additional water molecule forms a coordination bond with metals and a delocalized hydrogen-bond with the hydroxyl group.

The evolution mechanism from mononuclear to binuclear rare-earth metal complexes might be summarized as follows. The addition of water to $H^{\bullet}M(OH)_3$ forms $H^{\bullet}M(OH)_3(H_2O)$, in which the radical feature is retained. However, upon the addition of the Sc atom to MO_3H_4 to produce binuclear complex $M_2O_3H_4$ (labeled IM11 in Fig. 5), the hydrogen radical first binds to the two metals and then undergoes isomerization to a hydride structure (labeled IM12 in Fig. 5). During the reactions of IM12 with the first two OH radicals, the hydride structures remain. The subsequent reaction with the third OH radical results in the formation of $M_2O_6H_7$, in which the hydrogen atom in the metal hydride unit is transformed into one hydrogen bond. Therefore, during the $MO_3H_4 \rightarrow M_2O_6H_7$ processes, the active hydrogen atom undergoes the evolution of the hydrogen radical → bridging hydrogen → metal hydride → hydrogen bond, indicative of reduced reactivity.

The mononuclear complexes MO_4H_6 (M = Sc, Y, La) with an $M(OH)_3$ plane as its basic skeleton, are highly relevant to the ultrathin 2D rare-earth nanomaterials of layered rare-earth hydroxides $M(OH)_3 \cdot nH_2O$,[15,17] and the coordination bonding fashion of water with $M(OH)_3$ is similar to that of the reported rare-earth single-atom catalysis system.[9,10] The hydrogen radical is the key intermediate in a variety of processes (*i.e.*, catalysis, molecular hydrogen production, and new particle formation), but it is difficult to detect because of its high reactivity and a very short lifetime. In this work, the feature of hydrogen radicals in the rare-earth single-atom complexes $H^{\bullet}M(OH)_3(H_2O)$ is fortunately observed under the presence of additional water, which would have important implications for understanding the solvation effects of the catalysts and would suggest that the ultrathin 2D rare-earth nanomaterials of layered rare-earth hydroxides have the potential to trap hydrogen radicals and participate in more chemical processes.

The binuclear complexes $M_2O_6H_7$ (M = Sc, Y, La) contain an $M_2(\mu_2\text{-}O)_2$ unit, which is reminiscent of the actual rare-earth metal oxide catalysts. In the formation of $M_2O_6H_7$ from MO_3H_4, three bonding modes of hydrogen atoms are involved with the reactivity order of η^1-H > μ_2-OH > η^1-OH. Such reduced reactivity of hydrogen atoms might contribute to reducing the activation energy of the dehydrogenation reaction of the hydrogen storage materials.[4–6] These three types of hydrogen atoms were also observed in the process of ethylene/acetylene hydrogenation catalyzed by CeO_2,[14] and the reactivity sequence was consistent with our results. The deactivation of the CeO_2 catalyst has been rationalized by the overproduction with the formation of strongly bound M–OH groups that are

difficult to remove from the surface.[14] Our findings imply that the formation of $M_2(\eta^1\text{-OH})(\eta^1\text{-OH}_2)$ unit or hydrogen-bonding networks on the surfaces may also deactivate the catalysts, which provides insights into the strategy for tuning the active sites.

4 Conclusions

In this work, MO_4H_6 and $M_2O_6H_7$ (M = Sc, Y, La) complexes were prepared by a laser–vaporization supersonic expansion cluster source. Infrared-vacuum ultraviolet (IR-VUV) spectroscopy combined with quantum chemical calculations indicates that the MO_4H_6 and $M_2O_6H_7$ complexes have the $H^{\bullet}M(OH)_3(\text{-}H_2O)$ and $M_2(\mu_2\text{-OH})_2(\eta^1\text{-OH})_3(\eta^1\text{-OH}_2)$ structures, respectively. The joint experimental and theoretical results reveal that the formation of $H^{\bullet}M(OH)_3(H_2O)$ and $M_2(\mu_2\text{-OH})_2(\eta^1\text{-OH})_3(\eta^1\text{-OH}_2)$ is both thermodynamically exothermic and kinetically facile in the gas phase. The feature of hydrogen radicals in the mononuclear complexes $H^{\bullet}M(OH)_3(H_2O)$ is found to be retained under the presence of additional water. The addition of a metal atom to $H^{\bullet}M(OH)_3$ and subsequent combination with water produces the binuclear complex $M_2(\mu_2\text{-OH})_2(\eta^1\text{-OH})_3(\eta^1\text{-OH}_2)$, by which the reactivity of active hydrogen is reduced during the evolution of hydrogen radical → bridging hydrogen → metal hydride → hydrogen bond. The present experimental technique has the potential for size-selected infrared spectroscopic studies on a large variety of reactions between small molecules and neutral clusters, which will help to understand the structure–reactivity relationship of catalysts with isolated metal atoms/clusters dispersed on supports.

Author contributions

Ling Jiang and Gang Li conceived the idea, supervised the project and presented the project outline, guided the entire experiment, and provided funding support. Tiantong Wang conducted the experiments, calculations, and data analysis and wrote the original draft. Shangdong Li, Wenhui Yan, and Shuai Jiang conducted the experiments and data analysis. Hua Xie provided some advice for the characterization and analysis. All authors discussed the results, commented on the manuscript, and contributed to the final polishing of the manuscript.

Conflicts of interest

There are no conflicts to declare.

Acknowledgements

The authors gratefully acknowledge the Dalian Coherent Light Source (DCLS) and Specreation Co., Ltd., for their support and assistance. This work was supported by the National Natural Science Foundation of China (grant no. 22125303, 92061203, 22373102, 22103082, 22273101, 22288201, and 21327901), the National Key Research and Development Program of China (2021YFA1400501), the Youth Innovation Promotion Association of the Chinese Academy of Sciences (CAS) (2020187), Innovation Program for Quantum Science and Technology (2021ZD0303304), CAS (GJJSTD20220001), Dalian Institute of Chemical Physics (DICP DCLS201702), and International Partnership Program of CAS (121421KYSB20170012).

Notes and references

1 M. Zimmermann and R. Anwander, Homoleptic Rare-Earth Metal Complexes Containing Ln-C σ-Bonds, *Chem. Rev.*, 2010, **110**, 6194–6259.
2 F. Saraci, V. Quezada-Novoa, P. R. Donnarumma and A. J. Howarth, Rare-Earth Metal–Organic Frameworks: From Structure to Applications, *Chem. Soc. Rev.*, 2020, **49**, 7949–7977.
3 A. Mehtab, J. Ahmed, S. M. Alshehri, Y. Mao and T. Ahmad, Rare Earth Doped Metal Oxide Nanoparticles for Photocatalysis: A Perspective, *Nanotechnology*, 2022, **33**, 142001.
4 K. Iwase, K. Sakaki, Y. Nakamura and E. Akiba, In Situ XRD Study of $La_2Ni_7H_{(X)}$ during Hydrogen Absorption–Desorption, *Inorg. Chem.*, 2013, **52**, 10105–10111.
5 Z. Yu, W. Zhang, Y. Zhang, Y. Fu, Y. Cheng, S. Guo, Y. Li and S. Han, Remarkable Kinetics of Novel $Ni@CeO_2$–MgH_2 Hydrogen Storage Composite, *Int. J. Hydrogen Energy*, 2022, **47**, 35352–35364.
6 H. Zhang, L. Bao, Y. Pan and J.-Y. Ge, Enhanced Hydrogen Storage Performances of Binary Mg-Y Nanoscale Particles, *Chem. Phys. Lett.*, 2022, **796**, 139573.
7 X. Wang, Y. Zhu, H. Li, J. M. Lee, Y. Tang and G. Fu, Rare-Earth Single-Atom Catalysts: A New Frontier in Photo/Electrocatalysis, *Small Methods*, 2022, **6**, e2200413.
8 S. Nundy, D. Tatar, J. Kojčinović, H. Ullah, A. Ghosh, T. K. Mallick, R. Meinusch, B. M. Smarsly, A. A. Tahir and I. Djerdj, Bandgap Engineering in Novel Fluorite-Type Rare Earth High-Entropy Oxides (RE-HEOs) with Computational and Experimental Validation for Photocatalytic Water Splitting Applications, *Adv. Sustain. Syst.*, 2022, **6**, 2200067.
9 F. He, H. Li, Y. Ding, K. Li, Y. Wang and Z. Wu, The Oxygen Reduction Reaction on Graphitic Carbon Nitride Supported Single Ce Atom and Ce_xPt_{6-X} Cluster Catalysts from First-Principles, *Carbon*, 2018, **130**, 636–644.
10 J. Liu, X. Kong, L. Zheng, X. Guo, X. Liu and J. Shui, Rare Earth Single-Atom Catalysts for Nitrogen and Carbon Dioxide Reduction, *ACS Nano*, 2020, **14**, 1093–1101.
11 J. Feng, X. Zhang, J. Wang, X. Ju, L. Liu and P. Chen, Applications of Rare Earth Oxides in Catalytic Ammonia Synthesis and Decomposition, *Catal. Sci. Technol.*, 2021, **11**, 6330–6343.
12 X. Liu, Y. Luo, C. Ling, Y. Shi, G. Zhan, H. Li, H. Gu, K. Wei, F. Guo, Z. Ai and L. Zhang, Rare Earth La Single Atoms Supported MoO_{3-X} for Efficient Photocatalytic Nitrogen Fixation, *Appl. Catal., B*, 2022, **301**, 120766.
13 N. Liu, D. Cao, W. Liu, H. Zhang, Y. Zhu, L. Chang, D. Wu and D. Cheng, Constructing La-Doped Ultrathin Co-Based Nanostructured Electrocatalysts for High-Performance Water Oxidation Process, *Int. J. Hydrogen Energy*, 2022, **47**, 14504–14514.

14 J. Moon, Y. Cheng, L. L. Daemen, M. Li, F. Polo-Garzon, A. J. Ramirez-Cuesta and Z. Wu, Discriminating the Role of Surface Hydride and Hydroxyl for Acetylene Semihydrogenation over Ceria through In Situ Neutron and Infrared Spectroscopy, *ACS Catal.*, 2020, **10**, 5278–5287.

15 J. Xu, X. Chen, Y. Xu, Y. Du and C. Yan, Ultrathin 2D Rare-Earth Nanomaterials: Compositions, Syntheses, and Applications, *Adv. Mater.*, 2020, **32**, 1806461.

16 B.-I. Lee, H. Jeong, J.-S. Bae and S.-H. Byeon, A Layered Polymorph of Rare Earth Hydroxides, *Chem. Commun.*, 2013, **49**, 6051–6053.

17 Y.-S. Yoon, S.-H. Byeon and I. S. Lee, Unexplored Thermal Transformation Behavior of Two-Dimensionally Bound Gadolinium Hydroxide Layers: Fabrication of Oriented Crystalline Films of Gadolinium Oxychloride Nanosheets Suitable for the Multicolor Luminescence with Color Tunability, *Adv. Mater.*, 2010, **22**, 3272–3276.

18 G. Abellan, G. Minguez Espallargas, G. Lorusso, M. Evangelisti and E. Coronado, Layered Gadolinium Hydroxides for Low-temperature Magnetic Cooling, *Chem. Commun.*, 2015, **51**, 14207–14210.

19 F. Gandara, J. Perles, N. Snejko, M. Iglesias, B. Gomez-Lor, E. Gutierrez-Puebla and M. A. Monge, Layered Rare-Earth Hydroxides: A Class of Pillared Crystalline Compounds for Intercalation Chemistry, *Angew. Chem., Int. Ed.*, 2006, **45**, 7998–8001.

20 L. Zhang, J. Dong and M. Zhou, Matrix-Isolation Fourier Transform Infrared and Theoretical Studies of Laser-Ablated Sc Atom Reactions with Water Molecules, *J. Phys. Chem. A*, 2000, **104**, 8882–8886.

21 J. Guo and J. M. Goodings, A Density Functional Study of The Structures and Ionization Energies of Some Scandium Compounds with Hydrogen and Oxygen, *J. Mol. Struct.: THEOCHEM*, 2001, **549**, 261–273.

22 J. Guo and J. M. Goodings, A Density-Functional Study of the Reaction of Neutral Scandium with Water, *Chem. Phys. Lett.*, 2001, **342**, 169–176.

23 D.-Y. Hwang and A. M. Mebel, Theoretical Study of the Reaction Mechanism of ScO with Molecular Hydrogen, *Chem. Phys. Lett.*, 2001, **341**, 393–399.

24 L. Zhang, L. Shao and M. Zhou, Reactions of Laser-Ablated Y and La Atoms With H_2O Infrared Spectra and Density Functional Calculations of The HMO, HMOH and $M(OH)_2$ Molecules in Solid Argon, *Chem. Phys.*, 2001, **272**, 27–36.

25 X. Wang and L. Andrews, Infrared Spectra and Density Functional Calculations for The $Sc(OH)_{2,3}$ and HOScO Molecules and the $Sc(OH)_2^+$ Cation in Solid Argon, *J. Phys. Chem. A*, 2006, **110**, 1850–1858.

26 J. Xu and M. Zhou, Reactions of Early Lanthanide Metal Atoms (Nd, Sm, Eu) with Water Molecules. A Matrix Isolation Infrared Spectroscopic and Theoretical Study, *J. Phys. Chem. A*, 2006, **110**, 10575–10582.

27 J. Xu, X. Jin and M. Zhou, Reactions of Late Lanthanide Metal Atoms with Water Molecules: A Matrix Isolation Infrared Spectroscopic and Theoretical Study, *J. Phys. Chem. A*, 2007, **111**, 7105–7111.

28 A. Fujishima and K. Honda, Electrochemical Photolysis of Water at a Semiconductor Electrode, *Nature*, 1972, **238**, 37–38.

29 A. Ali, F. Long and P. K. Shen, Innovative Strategies for Overall Water Splitting Using Nanostructured Transition Metal Electrocatalysts, *Electrochem. Energy Rev.*, 2023, **6**, 1.

30 S. Jiang, H. Zheng, W. Yan, T. Wang, C. Wang, S. Li, H. Xie, G. Li, X. Zheng, H. Fan, X. Yang and L. Jiang, Capturing Hydrogen Radicals by Neutral Metal Hydroxides, *J. Phys. Chem. Lett.*, 2023, **14**, 2481–2486.

31 S. Jiang, H. Zheng, W. Yan, T. Wang, C. Wang, Y. Zhao, H. Xie, G. Li, X. Zheng, H. Fan and L. Jiang, Spectroscopic Identification of Water Splitting by Neutral Group 3 Metals, *Chin. Chem. Lett.*, 2023, **34**, 108244.

32 B. Zhang, Y. Yu, Z. Zhang, Y. Y. Zhang, S. Jiang, Q. Li, S. Yang, H. S. Hu, W. Zhang, D. Dai, G. Wu, J. Li, D. H. Zhang, X. Yang and L. Jiang, Infrared Spectroscopy of Neutral Water Dimer Based on a Tunable Vacuum Ultraviolet Free Electron Laser, *J. Phys. Chem. Lett.*, 2020, **11**, 851–855.

33 G. Li, C. Wang, H.-J. Zheng, T.-T. Wang, H. Xie, X.-M. Yang and L. Jiang, Infrared Spectroscopy of Neutral Clusters Based on a Vacuum Ultraviolet Free Electron Laser, *Chin. J. Chem. Phys.*, 2021, **34**, 51–60.

34 H. Zheng, S. Jiang, W. Yan, T. Wang, S. Li, H. Xie, G. Li, X. Yang and L. Jiang, Size-Specific Infrared Spectroscopic Study of the Reactions between Water Molecules and Neutral Vanadium Dimer: Evidence for Water Splitting, *J. Phys. Chem. Lett.*, 2023, **14**, 3878–3883.

35 M. J. Frisch, G. W. Trucks, H. B. Schlegel, G. E. Scuseria, M. A. Robb, J. R. Cheeseman, G. Scalmani, V. Barone, G. A. Petersson, H. Nakatsuji, X. Li, M. Caricato, A. V. Marenich, J. Bloino, B. G. Janesko, R. Gomperts, B. Mennucci, H. P. Hratchian, J. V. Ortiz, A. F. Izmaylov, J. L. Sonnenberg, D. Williams-Young, F. Ding, F. Lipparini, F. Egidi, J. Goings, B. Peng, A. Petrone, T. Henderson, D. Ranasinghe, V. G. Zakrzewski, J. Gao, N. Rega, G. Zheng, W. Liang, M. Hada, M. Ehara, K. Toyota, R. Fukuda, J. Hasegawa, M. Ishida, T. Nakajima, Y. Honda, O. Kitao, H. Nakai, T. Vreven, K. Throssell, J. A. Montgomery Jr, J. E. Peralta, F. Ogliaro, M. J. Bearpark, J. J. Heyd, E. N. Brothers, K. N. Kudin, V. N. Staroverov, T. A. Keith, R. Kobayashi, J. Normand, K. Raghavachari, A. P. Rendell, J. C. Burant, S. S. Iyengar, J. Tomasi, M. Cossi, J. M. Millam, M. Klene, C. Adamo, R. Cammi, J. W. Ochterski, R. L. Martin, K. Morokuma, O. Farkas, J. B. Foresman and D. J. Fox, *Gaussian 16 Rev*. A.03, Wallingford, CT, 2016.

36 D. O. Kashinski, G. M. Chase, R. G. Nelson, O. E. Di Nallo, A. N. Scales, D. L. VanderLey and E. F. Byrd, Harmonic Vibrational Frequencies: Approximate Global Scaling Factors for TPSS, M06, and M11 Functional Families Using Several Common Basis Sets, *J. Phys. Chem. A*, 2017, **121**, 2265–2273.

37 S. Feyel, J. Dobler, R. Hockendorf, M. K. Beyer, J. Sauer and H. Schwarz, Activation of Methane By Oligomeric $(Al_2O_3)_x^+$ (x = 3,4,5): The Role of Oxygen-Centered Radicals in Thermal

Hydrogen-Atom Abstraction, *Angew. Chem., Int. Ed.*, 2008, **47**, 1946–1950.

38 X. N. Wu, Y. X. Zhao, W. Xue, Z. C. Wang, S. G. He and X. L. Ding, Active Sites of Stoichiometric Cerium Oxide Cations ($Ce_mO_{2m}^+$) Probed by Reactions with Carbon Monoxide and Small Hydrocarbon Molecules, *Phys. Chem. Chem. Phys.*, 2010, **12**, 3984–3997.

39 Y.-X. Zhao, X.-N. Wu, J.-B. Ma, S.-G. He and X.-L. Ding, Experimental and Theoretical Study of the Reactions between Vanadium–Silicon Heteronuclear Oxide Cluster Anions with *n*-Butane, *J. Phys. Chem. C*, 2010, **114**, 12271–12279.